Integrative and Comparative Biology

Integrative and Comparative Biology, volume 62, number 4, pp. 1085–1095
https://doi.org/10.1093/icb/icac053

Society for Integrative and Comparative Biology

SYMPOSIUM

Use of the LunAero Open-Source Hardware Platform to Enhance the Accuracy and Precision of Traditional Nocturnal Migration Bird Counts

Wesley T. Honeycutt[1] and Eli S. Bridge

Oklahoma Biological Survey, University of Oklahoma, 111 Chesapeake, OK 73019, USA

From the symposium "Open source solutions in experimental design" presented at the annual meeting of the Society for Integrative and Comparative Biology virtual annual meeting, January 3–February 28, 2022.

[1]E-mail: honeycutt@ou.edu

Synopsis Quantification of nocturnal migration of birds through moon watching is a technique ripe for modernization with superior computational power. In this paper, collected by a motorized telescope mount was data analyzed using both video observations by trained observers and modernized approaches using computer vision. The more advanced data extraction used the OpenCV library of computer vision tools to identify bird silhouettes by means of image stabilization and background subtraction. The silhouettes were sanitized and analyzed in sequence to produce stacked relationships between temporally close contours, discriminating birds from noise based on the assumption that birds migrate in stable paths. The flight ceiling of the birds was determined by extracting relevant correlation coefficient data from doppler radar co-located with the LunAero instrument in Norman, OK, USA using a method with low-computational overhead. The bird paths and flight ceiling were combined with lunar ephemera to provide input for the original method used for nocturnal migration quantification as well as an enhanced version of the same method with more advanced computational tools. We found that the manual quantification of migration activity detected 16,300 birds/km•h heading northwest from 110°, whereas the automated analysis reported a density of 43,794 birds/km•h heading northwest from 106.67°. Hence, there was agreement with regard to flight direction, but the automated method overestimated migration density by approximately three times. The reasons for the discrepancy between flight path detection appeared to be due to a substantial amount of noise in the video data as well as a tendency for the computer vision analysis to split single flight paths into two or more segments. The authors discuss ongoing innovations aimed at addressing these methodological challenges.

Introduction

The annual cycle of bird migration is one of largest redistributions of biomass on the planet (Somveille et al. 2015; Møller and Szép 2011). However, it is difficult to give a precise estimate of the extent of aerial migration, leading to one of the grand challenges in migration ecology: "How many and which animals are aerially migrating?" One means of addressing this challenge is an observational method known as "moonwatching."

Moonwatching was originally described to academic literature by W. E. D. Scott in 1881 accompanying an estimate of flight altitude after a fortuitous observation of the moon during an astronomy demonstration (Scott 1881). This observation of nocturnal migration was a notable demonstration of the "how" question implicitly posed by confirmation of bird migration by Scott's contemporaries (Richter and Bick 2018; Jenner 1824). A review of various reported observations of nocturnal migration from that era are historical summarized in a short paper by Fredric Carpenter (Carpenter 1906). The technique of ornithological moon watching became advanced over time, culminating in codified mathematics to ascertain flight direction and estimation of nightly counts detailed by George H. Lowery (Lowery 1951) and practically assessed by Ian C. T. Nesbit (Nisbet

Advance Access publication June 1, 2022

1959). However, the idea of staying up all night to watch birds quickly faded from prominence as radar-based methods of quantifying bird migration were introduced, which correlated the data from each tool (Nisbet 1963).

Early operators of radar stations observed unexpected echoes dubbed “angels” (Gould 1947), which went unreported until 1945 due to the wartime secrecy surrounding radar (Lack and Varley 1945; Harper and Lack 1958). As the technology was refined, radar has become one of the most important tools to study avian migration (Chilson et al. 2011), ostensibly producing more quantitative data in a single night than an ornithologically minded astronomer might produce in a whole season. However, radar studies do not give the whole picture. Environmental factors such as terrain, foliage, and local weather can influence the echoed signals (Chilson et al. 2011; O’Neal et al. 2010). While previous studies have found a significant correlation between radar echoes associated with birds and traditional observations, they also report notable variations in the data (Gauthreaux 1970; Farnsworth et al. 2004; Komenda-Zehnder et al. 2010). Advances in radar analysis technology for biological backscatter (bioscatter) have led to improved detection methods in recent years (Bachmann and Zrnić 2007; Zaugg et al. 2008; Lakshmanan et al. 2015), but the techniques still rely heavily on *a priori* knowledge such as roost locations and migration pathways (Russell et al. 1998; Winkler 2006). Importantly, weather radar alone does not allow for inferences about species identification or social behavior, as all aerial biomass is detected as a summation of reflected radio waves from different air volumes. Other radar technologies such as marine and tracking radar are able to resolve some of these behaviors, but they are often prohibitively expensive. Lunar observation of nocturnal migration has been correlated with narrow-beam radar data, demonstrating the usefulness of lunar observation within reasonable limitations for ground-truthing (Liechti et al. 1995). Liechti *et al.* note that lunar observation of nocturnal migration is a cost-effective technique which can be deployed on a large scale, although they also point out that human observers often fail to observe many of the birds detected by radar. Yet, lunar observations provide more granular detail than observed by other techniques, providing information on flight grouping, behaviors, and limited genus-level identification. Early pioneers first recognized radar angels represented groups of birds rather than individuals Nisbet (1963). Visual observations provide insight into the number and nature of birds flying in groups greater than achieved by any other method, and there remains much to be learned about the number, type, how, and when birds form these groups that can only be learned through direct observation.

We recently described a hardware platform for moonwatching, which we refer to as “LunAero” (Honeycutt et al. 2020). In leiu of using a commercial telescope system with a motorized mount, we developed LunAero to be a low-cost, open source device that might encourage participation by citizen scientists and bird enthusiasts. The video footage collected for the current study was from one of our preliminary LunAero designs that featured a Raspberry Pi computer equipped with an inexpensive camera module mounted to a spotting scope. The computer used simple machine vision techniques to track the position of the moon in the video frame while controlling a motorized mount for the spotting scope to maintain a full view of the moon. The computer simultaneously recorded video data to a portable USB thumb drive at 30 frames per second with 1080 × 1920 pixel resolution. The video footage was subjected to a frame-by-frame analysis which applied computer vision to detect bird silhouettes and assemble them across frames into bird flight paths. We compared three combinations of detection and analysis methods: (1) manually watched video with Lowery’s calculation techniques, (2) birds detected by the computer vision algorithm with Lowery’s calculation techniques, and (3) birds detected by the computer vision algorithm with an advanced form of projection geometry, with the expectation that there would be marked improvements associated with the use of modern computing.

Methods

The video footage used in the current study came from a preliminary version of the LunAero device (Honeycutt et al. 2020) deployed in the northern outskirts of Norman, Oklahoma that collected approximately 1.5 h of video footage on April 28, 2018 beginning at 9:00 PM CDT using a 40x ATS 65 spotting scope (Swarovski Optik, Absam, Austria). LunAero operated independently of human intervention, including observers, during the specified time. Three different observers were employed to parse through this segment of video frame-by-frame to denote every visible bird silhouette, and we regard the summation of these observation as the “known” set of bird flight paths from this video segment. Individual observers watched video using VLC media player on a computer monitor consistent through all tests. The observers were allowed to watch video as quickly or as slowly as they required, and they were encouraged to rewind the video to confirm observations frame-by-frame, especially to ensure the observer noted the first and final appearance of the silhouette. Observers recorded the timestamp of each silhouette, the location on the lunar face where the silhouette first appeared, and a general heading. A flight path of moving silhouette was noted as the viewable silhouette between first appearance and disappearance from the lunar disk with exceptions given for silhouettes that temporarily disappeared in the lunar albedo which obviously belonged to the same bird as determined by the visual observer. Mismatches between observed silhouettes were confirmed by the author, WTH, in cooperation with the original observer to rectify the missed silhouettes. The timestamps of the appearance and disappearance confirmed silhouettes were converted to frame numbers since the start of the video for comparison to the output from the computer vision algorithm. Based on the silhouette timings manually observed in the video, we emulated the method outlined by Lowery to calculate the net motion and flight density from the sample.

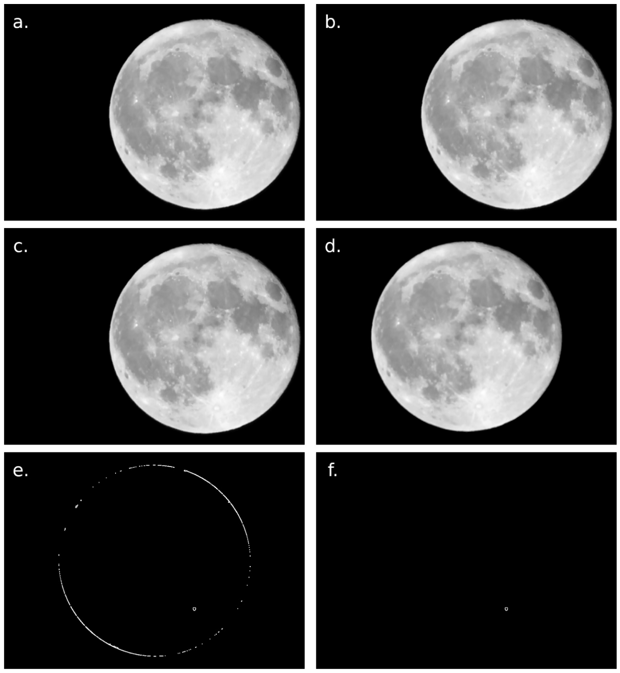

Fig. 1 This image shows a composite of the steps taken to extract contours of silhouettes from the input video. Our code converts the original frame **(a)** into grayscale **(b)** and performs a blurring operation **(c)**. Using the largest contour, that of the lunar surface, the script centers the moon to account for video stability **(d)**. Subtracting the surface features of the moon, only contours which have changed between frames remain **(e)**. By masking the shimmering edge of the moon, we are left with a single bird silhouette contour **(f)**. Note that this example represents the ideal performance

Computer vision video analysis

For this implementation, image processing occurs using a set of scripts written for Python3 on previously recorded videos. The majority of the scripts functions are called from imported OpenCV, a computer vision framework which provides frequently used operations in an easy-to-use format, and Numpy, a package for vectorized operations, modules which handle the requisite image processing and math, respectively (Bradski 2000; Oliphant 2006). OpenCV opens the stored video file and reads it frame-by-frame. During the course of a standard loop of operation, the following general steps are performed:

(1) The extracted frame is sanitized of noise and fit to a standard format.
(2) The program identifies objects which move with respect to the background.
(3) A ring buffer acts as temporary storage for the information about these identified objects.
(4) Assuming the ring buffer is filled, object information is compared across frames to search for patterns.
(5) The loop restarts or reports that the final frame has been processed.

In each frame cycle, OpenCV handles image-processing steps to produce data. The code converts each sequential frame into grayscale and blurs the moon using a 5×5 Gaussian kernel, which will not obscure small bird silhouettes; later object detection steps operate based on luminosity difference, which remains with such minor blurring. Using the largest object detected in the image, the code centers the moon on a black background by conic fitting (Fitzgibbon and Fisher 1995). A buffer running in the background keeps the most recent images in memory, which we use to subtract everything unchanged in the frame (KaewTraKulPong and Bowden 2002). This leaves bird silhouettes in motion and any shimmering noise on the frame. Since the edge of the moon against the sky constantly shimmers, it does not perfectly subtract during the background removal step. We simply draw a black halo around the edge of the moon to omit these erroneous detection. These steps visually represented by example in Fig. 1. Details of these steps are described in more detail in Appendix A and archived as code at https://github.com/BlueNalgene/Birdtracker_LunAero.

Once the image of the moon is centered and processed within the frame, OpenCV is used to determine the contours present. As the moon was artificially centered on a background with luminosity of 0, and the majority of the lunar features were removed during the background subtraction, it is trivial to determine that the contour function should only include pixels which have a nonzero luminosity. The contours are, therefore, distinct and can be interpreted by the Suzuki et al. method (Suzuki and be 1985). Despite best efforts to

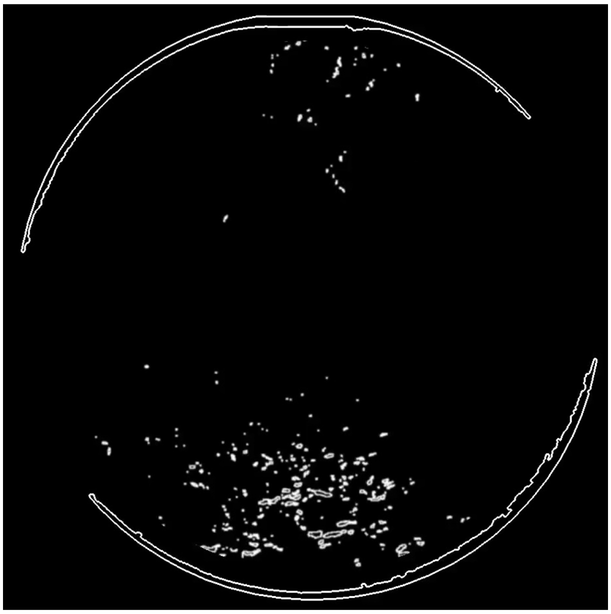

Fig. 2 Unlike the ideal example shown previously, this shows a much more common output from the script. This image, captured prior to the halo masking step, shows a very cluttered moon. In this case, atmospheric scintillation caused the lunar mare to change luminosity between the prior frames and this one. Other examples exist where turret movement during LunAero's tracking motion causes a similar appearance due to shearing. Despite the high noise, this frame represents a "hit." The contour of a bird silhouette hides somewhere among the other noise in this image. Correctly identifying this silhouette is left as a challenge to the reader to demonstrate the difficulty for naive computational power to detect small flying objects. The correct answer is given in Supplementary Fig. 6

minimize extraneous contours from the input, OpenCV detects many more contours than those attributable to bird silhouettes, as shown in Fig. 2. Instrumental vibration instability, backlash in gears introduced by low-cost fabrication techniques, and atmospheric scintillation by localized turbulence (Andrews et al. 1999; Osborn et al. 2015) conspire to introduce minuscule distortions near the surface and mare features of the moon, especially during camera slew. Computer vision cannot yet identify moving objects without a comparative frame of reference. By this, we mean that there must be some separable distinction between true and false bird silhouettes in static imagery such as contour radius, definable shape, color change, or shadowing. In the case of LunAero and moonwatching, bird silhouettes are so small and indistinct that we are forced to rely upon interframe differences for motion detection, rendering current paradigms in machine learning based object detection useless. Instead, we must rely on specialized naive computer vision algorithms. Attributions of and potential solutions to noisy output is subject to intense study in computer vision; however, for the purpose of this experiment, we use an easily repeatable contour detection method provided in the OpenCV framework.

Buffer operations to detect linear motion

To distinguish contours detected by the OpenCV operation, we classified contours as "hits" if they followed a near linear path. We based the assumption of a linear path of all birds during migration on:

(1) narrow shape of the conic sampling window,
(2) high altitude shape of the same cone, and
(3) video capture at a rate of 30 frames per second.

Using this assumption, we exclude many erroneous detections by computer vision: a track of detected contours that forms an exaggerated "V" shape in three frames is more likely due to the lunar surface than due to a particularly mobile bird. True birds flying in the narrow conic window fly in relatively linear paths, staying at a constant altitude and speed within the small sample. While flapping and shape deformation caused by image quality and pixelation make the linear travel appear imperfect under ideal circumstances, any deviations occur within bounds. However, this assumption is imperfect. The high altitude reach of the sampling cone limits the influence of migrating insects on the collected silhouettes, only those which fly very close to LunAero appear in the video. However, since these insects fly close to the camera, we easily observe the less stable flight patterns, as in the case of a large beetle which wobbles across the test video, making them easy to distinguish from birds. Similarly, non-migrating insectivores (bats, swifts, etc.) are also easily distinguished from the level-flying migrants by their swooping paths, but only with sufficient framerate to detect such motion. While the authors observed no instances of man-made flying objects during this study, other video segments uncommonly contain distinct planes. Some non-birds may fly straight and some birds may fly less than linear paths. Further work will reveal more accurate behavioral traits which will produce more accurate tracks, but the simplicity of the linear flight assumption must serve for now.

The computer vision analysis and linear motion detection script operated on the 1080p video segment recorded in 2018 using the University of Oklahoma's (OU) Supercomputing Center for Education & Research with a single Intel Xeon "Haswell" E5-2650v3 10-core 2.3 GHz node with 32 GB RAM. During video processing, the code records the position and bounding radius of each contour detected to a ring buffer of the latest three frames, along with the frame number since the video began recording. From these intrinsic properties of the contour, the code calculates several derived products based on contours detected in a previous frame: contour displacement (d), radial size change (Δr), and apparent direction (τ). The code stacks these newly calculated derived products and compares them with previous values. The details of these calculations and comparisons are reported in Appendix B. Only those values deemed within tolerance bounds across three frames for d, Δr, and τ remain when the ring buffer cycles to open a new frame. The data that remain represent likely "hits" on bird silhouettes. As the intention of this paper focuses on the birds and their flight paths, we have opted to eschew the traditional computer vision object detection metrics such as mean average precision (mAP) and precision–recall (PR) curves, averting deep delves into computer vision.

We assume birds continually exist, not blink in and out of reality: One bird crossing the moon should produce an entry for each subsequent frame in which it appears in the frame, although we will discuss the unpleasant failings of this assumption later in the paper. The steps described stack probable hits based on data from the previous two frames, but those steps are naive to connections beyond three frames. Without the persistent bird assumption, we find longer range geometries between silhouette results. This assumption performs poorly when the original silhouette detection missed a portion of the track. This case becomes especially problematic when the luminosity of the moon appears oversaturated, as silhouettes become lost in the brightness. Therefore, the current persistent bird assumption remains video quality dependent. The best way to ensure high-quality output is production of high-quality input. While well-intentioned, this maxim often fails to hold with LunAero, as changes in the atmospheric conditions fluctuate. A perfect scene quickly turns to an over-bright one as the water content in the column of air between the observer and the moon decreases. Live adjustment of frame brightness on the LunAero hardware would solve this problem but introduce new problems, as brightness on inexpensive rolling shutter style cameras directly relates to shutter speed, which would cause the bitrate and temporal precision of the video to fluctuate with these adjustments. An ideal solution during post-capture video analysis would use predictive placement of silhouettes which cross the moon, allowing the code to guess that a bird in linear motion based on the apparent crossing speed and direction of the contour at the first frame. However, such a "Kalman filter" approach to silhouette detection becomes $\mathcal{O}\left(n^3\right)$ computationally complex, making it non-trivial for long videos.

Modernized lowery method

Co-location with KTLX weather radar

The original Lowery technique involves an estimation of the upper limit or the "flight ceiling" for the birds observed. This estimation amounted to a reasoned guess by the observer. We may reduce the error associated with this approximation by establishing a more precise flight ceiling based on radar observation of bioscatter.

Conveniently, Norman, OK, sits within the radius of the KTLX weather radar installation, which covers altitudes below 1 km (Maddox et al. 2002). Calculation based on radar data reveals that our field site was covered above 165 m, although since this site is the location of the LunAero deployment, the relevant coverage information is relative to the azimuth of the moon. While this means that the coverage is biased against detecting takeoff and touchdown of migrants, it is sufficient to determine cruising altitudes at this deployment (Horton et al. 2019).

To do so, we accessed Level 2 weather radar data from Next Generation Weather Radar (NEXRAD) on Amazon Web Services (https://registry.opendata.aws/noaa-nexrad) and extracted the correlation coefficient (ρ_{hv}) data product for 10 radar scans that correspond to the time of video data collection and the air volume surrounding the field site out to a radius of 300 km. The correlation coefficient measurement assesses the "sameness" of signals within a range gate as detected by the dual-polarized beams of the current NEXRAD installations. Biological entities typically have lower correlation coefficient values than more uniform non-biological objects like rain drops. To facilitate acquisition of average flight altitudes, a GUI implementation was developed using the Python ARM Radar Toolkit to perform a visual check of the rho_{hv} band pass filter and geographic areas excluded as ground clutter, as seen in Fig. 3. We selected band pass values for ρ_{hv} and radial distance from the instrument r to sample data outside of the ground clutter region and with heterogeneous echo signatures, sampling the entire airspace covered by KTLX outside the ground clutter. Using additional animation of the ρ_{hv} radar data around this time point, we graphically observed the relative motion of radar signals visually distinguish weather phenomena from aerial migrants. We saved the average radar gate altitude $\bar{h}$ associated with data retained from the filters as our flight altitude (Fig. 4).

Elliptical projection and flight paths

The method of projection of silhouettes onto a geodesic system adheres to many of the same steps as those established by Lowery. The "great cone," which points its apex toward the observer and base toward the moon, when flattened, provides the heading of birds passing through that section of the night sky. Modern computational power allows us to skip many of the requisite shortcuts in the original Lowery method, notably the "clock face" reckoning of motion which limits the pre-

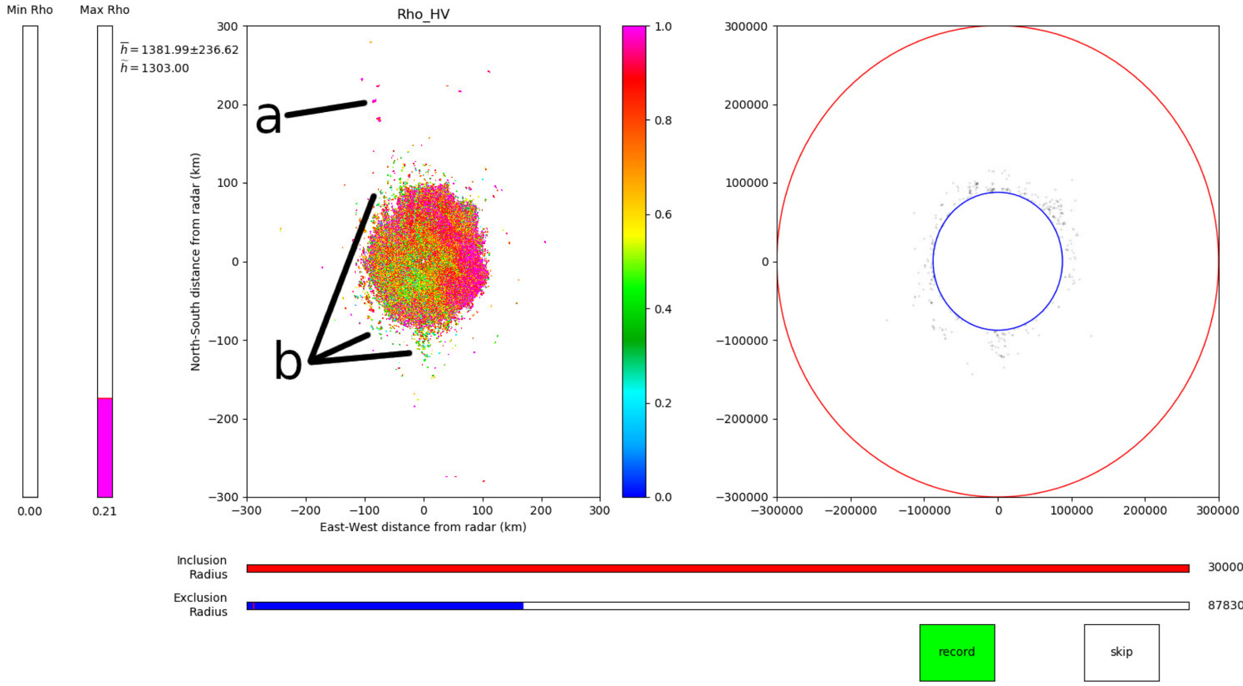

Fig. 3 This figure depicts one example of the Python GUI developed to extract radar echoes with low correlation coefficients (ρ_{hv}) with radial exclusion zones to prevent collection of ground clutter. In this example, the ρ_{hv} data product from a Level 2 radar archive from KTLX installation appears on the left. The plot with circles, which appear on the right of the graphic, depicts a visualization of the script's output. Sliders on the extreme left of the image allow the user to adjust the band pass filter for the values of ρ_{hv} from the original data. In this example, we include $0 < \rho_{hv} \leq 0.21$. Similarly, the sliders on the bottom of the screen allow the user to adjust the exclusion radii r of the outer and inner circles. In this example, we include $87830.69 < r \leq 300{,}000$. The combination of these two band pass filters for ρ_{hv} and r produces the grayscale points between the colorful exclusion radii on the rightmost plot, respectively. The average (with standard deviation) and median height are updated to the user on the top left of the figure in purposefully small text to prevent focusing on error reduction for band pass filter selection. Points from the original data set have been superficially labeled noting (a) points with high ρ_{hv} values, which appear to be moving westward during radar plot animation, and (b) points with low ρ_{hv} near the edge of the ground clutter radius which appear to be moving northward during animation. Pressing the "record" button records data to an output file; "skip" moves to the next entry without recording the output

cision of input silhouette tracks to $\pm 15^{\circ}$. Similarly, our computational power allows us to process data recorded on nights farther from the full moon phase. The same circular moon assumptions made by Lowery still apply during periods where the fullness of the moon exceeds the resolving power of the telescope, such as the night of video we analyze in this paper. As this part of the technique is not essential to the data at hand, we explore it more fully in Appendix C.

For a circular moon, we require the observation time (t), the average radius of the moon ($\overline{r_{moon}}$), and the topocentric location of the observer (latitude, longitude, elevation). Using these inputs, the Python package astropy automatically calculates the lunar position relative to the observer using ephemera from the Jet Propulsion Laboratory (Astropy Collaboration et al. 2013, 2018; Rhodes et al. 2019), importantly these include altitude (alt), azimuth (az), and the distance to the moon from the observer d_{moon}. The right, circular cone pointing its apex from the observer to the moon has a slant length of

$$\ell = \arctan \frac{d_{moon}}{\overline{r_{moon}}}, \tag{1}$$

which yields an elliptical shape relative to the atmosphere with an eccentricity

$$\mathrm{ecc} = \frac{\sin alt}{\sin \ell}. \tag{2}$$

The distance from the observer to the center of the ellipse representing the average flight altitude of birds from radar observation is found by

$$d = \frac{\bar{h}}{\tan \mathrm{alt}}, \tag{3}$$

which we must convert to an elliptical projection. This project has a semi-minor axis equal to the radius of our circular spot at flight altitude

$$r_{\mathrm{min}=\frac{d}{\tan \mathrm{alt}}} \tag{4}$$

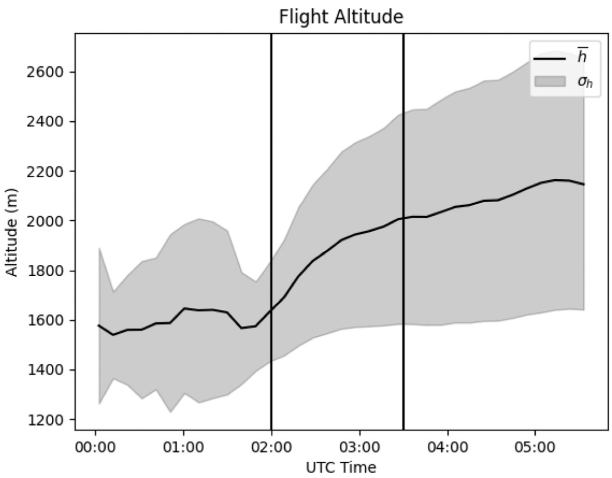

Fig. 4 The average flight altitude on the night of April 28, 2018 from midnight UTC as calculated by the method outlined in the section plotted with interpolation between scans every 10 minutes shows the increasing altitude of bioscatter from KTLX as the night progresses. This example plot was generated using the Python script to filter radar gates with several values set prior to the calculation for demonstration purposes. The vertical lines bound the recording time of the video used in this analysis, and the surrounding data added to provide context. In this plot, the parameters for the band pass filters were locked at r_{min} =10,000 m, r_{max} =300,000 m, $\rho_{hvmin} = 0.1$, and $\rho_{hvmax} = 0.5$. Generally, the standard deviation of echo altitudes around the mean is directly related to the observed altitude.

and the major axis found by eccentricity

$$r_{\mathrm{maj}} = r_{\mathrm{min} \times \sqrt{1-\mathrm{ecc}^2}}. \quad (5)$$

Treatment of this flattened ellipse in parallel to the "plane" of a flat earth project similar to a gnomonic projection returns the parallel flight path of bird silhouettes, which we ascribe here as η' to denote a deviation from Lowery's original projection techniques. We find the path the bird travels as

$$\theta = 180^\circ + \left(2 * \arctan \frac{\tan \eta' - \mathrm{az}}{\cos 90^\circ - \mathrm{alt}}\right), \quad (6)$$

mirroring the result relative to the topographic perspective, with the 180° rotational symmetry operation.

Lowery used vector representations of outputs of his bins like those in Fig. 5b to calculate the net trend of bird tracks or the general heading of birds in the sampling window. Using the count of birds as magnitude of vectors and the heading of the bin, we take the weighted average of every detected bird. Lowery's bins have unequal size, making it unlike a histogram. The unequal size arises from Lowery's handling of the elliptical projection out of necessity for computational simplicity; by scrunching up bins near the minor axis of the projected ellipse and stretching out bins near the major axis, Lowery avoids the challenging math required for equal project. Lowery calculates sector centerline projected on the earth for his bins with

$$\theta = \arctan \frac{\tan(\eta - \mathrm{az})}{\cos Z}, \quad (7)$$

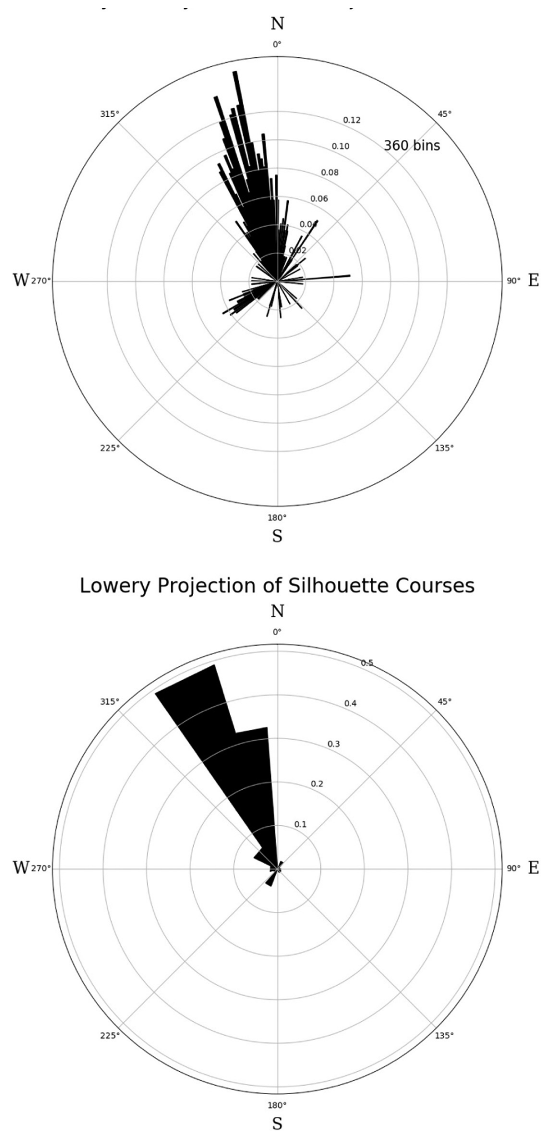

Fig. 5 This figure compares the granularity of the new approach to bird tracking with the Lowery method. Both figures show a normalized distribution of birds on with respect to compass direction. The first figure groups the bird silhouette data in 360 equal-sized bins (each 1°) from the new method. The Lowery method in the second figure creates 16 unequal-sized bins rather than the equivalent bins in the form of a polar histogram. In addition to the lower precision due to less bins in the Lowery method, this bin sizing also creates distinct variation in accuracy, artificially weighting the error in favor of bins perpendicular to the declination of the moon. Both plots use the same input data collected by the computer vision script. The "truth" of the Lowery plot created by human observation of the recorded video, rather than computer vision, may be found in the authors' previous work (Honeycutt et al. 2020)

where η represents the true compass heading that each sector represents and Z represents the lunar zenith angle:

$$Z = 180^{\circ} - \text{alt}. \tag{8}$$

We subvert the intent of this equation to solve for the compass heading of each bird. Lowery only calculated his method 8 times per hour for 16 bins (reflecting over the centerline of the circular moon), but with our better computational ability, we calculate the track for individual birds with temporal accuracy of Z and az dependent solely on the framerate of the video using ephemeral calculations for the moon. The enhancement increases the precision of measurements temporally, as we report down to the 1/30th of a second, and spatially, as the ephemeral calculation produces more precise lunar positions. We further enhance spatial precision by flight ceiling adjustment based on the radar altitude estimator. We report our data as a polar histogram with traditional compass headings using an arbitrary yet convenient 360 bins.

Our bird density estimates arise from

$$D = \frac{\delta n \cos^2 Z}{\sqrt{1 - \sin^2 Z \cos^2 \alpha}}, \tag{9}$$

where δ represents a complete lunar distance angle:

$$\delta = \frac{2}{\arcsin \frac{d_{lunar}}{d}}, \tag{10}$$

and α represents the angle between the flight path and the lunar position reckoned from the south such that

$$\alpha = 180^{\circ} - \eta + \text{az}. \tag{11}$$

To minimize computational complexity, Lowery simplifies δ to 220, a value with three significant figures. We present results where the calculation of δ becomes trivial due to computational ephemera, granting us greater precision. Since we choose to not use Lowery's η in the modern technique, we instead calculate α from the center line of the arbitrarily large bins in the polar coordinate plane. (For our 360 bin example in Fig. 5a, the η values become 0.5°, 1.5°, 2.5°, $\ldots 355.5^{\circ}$.) Therefore, our analytical design will produce results with greater precision than the original technique.

Results and discussion

The 1.5 h sample of video footage yielded a sum total of 450 birds observed (300 birds/h). These birds mostly moved in a northwesterly direction (reckoned 110° north of east) with a total flight density 14,193 birds/km•h. The flight paths were represented by as few as a single frame and silhouettes often appeared as a single pixel *in extrema*. Each of the three video observer's results were compiled, and discrepancies between listed observations were rectified as a group. Video inspection time amounted to about 15 h for each observer. The time required for the automated extraction of flight paths was approximately 8 h. Hence, the computational approach was somewhat faster than manual analysis. However, the automated method reported 1340 detected flight paths that included at least three silhouettes across separate video frames. These flight paths were compiled from 783,459 groups of pixels that were interpreted to be potential bird silhouettes. The computer vision identified 663 frames containing birds correctly and reported 298 as false positives. Counting contours rather than tracks, the computer identified 8.45% of all frames with birds that a human found. While this number appears low, the computer correctly identified 46.6% bird tracks in the video.

The data collected by the computer vision algorithm are summarized in Fig. 5 in the form of both a histogram with relatively high angular precision using the modern analysis technique discussed in section and in the form described by Lowery. When this dataset was manually analyzed, we found that the net trend density (ρ_{net}) of migrants in the video based on Lowery's original method as 16,300 birds/km•h heading 110° reckoned north of east. When we process the results from the computer vision analysis performed here with the same Lowery method, we observe ρ_{net} as 54,700 birds/km•h heading 107° reckoned north of east. Using the same dataset but with the modern technique, we observe ρ_{net} as 43,794 birds/km•h heading 106.67° reckoned north of east (The significant figures which we use to report values depend on calculation techniques.)

While our automated method of quantifying migratory activity seems to work well for determining the mean flight direction, it clearly overestimates the number of flight paths detected, indicating there are shortcomings of the computer vision analysis presented here. In addition to the evident problem of too many "false positives" in the automated analysis output, we also see that many of the "real" tracks observed during manual video inspections do not appear in the computer vision output. Moreover, it is apparent that some of the inflation of the number of flight paths is due to repeated tracks, wherein the same silhouettes are recruited into the construction of several different flight paths. If we sift through the tracks to remove coincident, sequential silhouette events across frames (e.g., when one track reports a silhouette moving across frames $n = 1$, $n = 2$, and $n = 3$), then another track reports a silhouette on frame n which overlaps the previous track's values for $n = 1$ and $n = 2$ position, we can assume that this is the same object in motion), the track count reduces to 961. A substantial portion of the discrepancy between the manual count and the automated count is due to false flight paths that arise due to noise in the video footage. Atmospheric scintillation problems and unstable camera motion appeared to lead to thousands of pixel clusters that were interpreted as potential bird silhouettes. Given the large numbers of false silhouette detection, the detection of false flight paths was inevitable, we saw more than half of the tracks here as false positives. Another substantial source of error was due to single flight paths being split into two. For many of the more distant birds, their silhouettes were sometimes invisible due to saturation by the bright background of the moon or because the birds adopted a folded-wing posture during flight (thus reducing its visible cross section). As a result flight paths often presented as several partial segments that were counted as different animals. Since computational complexity increases by $\mathcal{O}\left(n^3\right)$ for Kalman filters or similar position guessing functions, it is computationally impractical to increase accuracy with this technique to correct for segmented flight paths during initial computer vision analysis.

Conclusion

In this paper, we have explored an incremental advancement in moonwatching for nocturnal migration analysis based on the LunAero open-source hardware platform. Our methods of collecting video in the field and analyzing the results offers an alternative to the time-intensive methods that preceded the widespread availability of computers. However, the automated method clearly requires further innovation to better align the detection of flight paths with what is apparent to a human observer performing an exhaustive frame-by-frame inspection of the video data. Birds, which sometimes appear as small as a single pixel in 1080 pixel video, can be nearly indistinguishable from lunar surface features, atmospheric scintillation introduced noise, and motion distortion artifacts even to the trained eyes of experienced birders. Inexpensive motors with simple gearing, opting to live center the moon rather than using ephemeral calculation with precise timing, and harsh backlash in laser cut gears conspire to cause twitchy, frequent readjustment of camera positions which, in turn, appears as stretching and tearing of frames in the video. These abnormalities in the frame appear as an object in motion to this naive background subtraction. In normal operation of background subtraction buffers for object detection, the objects tracked by the computer vision appear much larger in the frame, e.g., a human walking by a security camera, allowing for simple correction techniques such as contour radius size exclusion which we do not use due to the small size of migrant silhouettes.

Currently, the authors toy with new strategies to overcome the existing weakness reported here including options to composite techniques for background subtraction and contour detection into a weighted algorithm, modified assumptions which change the sampling window of the great cone projected from the instrument i.e., a shallow cone means small birds fly too high to be counted, LiDAR co-location to provide a secondary data source, and other techniques which would serve to enhance the accuracy of LunAero data. Running a cloud computation implementation for video data would cost considerably less than a trained human, rendering it feasible to deploy a tightly spaced array of LunAero units at a single site to detect migrants in coordination and analyze this greater output of raw video. Similarly, distributed LunAero deployments, e.g., co-located with all WSR-88D in the USA or at every wind farm in a region, would produce large datasets on the widely spread migration with the network still producing data while some units shut down due to cloudy conditions. Preliminary efforts to enhance the automated analysis method have shown that a series of simple post-hoc filters that take into account the number and spatial distribution of silhouettes that comprise a flight path can eliminate many of the false positives that result from the computer vision analysis. We have also implemented methods that rank the likelihood that a potential silhouette is, in fact, produced by a bird, and theses rankings figure into discerning true flight paths from false detections. Similarly, we have implemented filters that detect separate flight paths that are likely to be segments of the same flight path. Paths flagged by these filters can simply be merged together to improve accuracy (E. Bridge, unpublished).

There is also potential for improvement through the modification of the LunAero hardware. Careful monitoring and adjustment of brightness levels can alleviate some of the problems associated with saturation of silhouettes, which often renders them undetectable. There is also room for improvement with regard to reducing image shakiness associated with the movement of the motorized turret. With gradual acceleration and deceleration of the movement, later versions of the Lunearo hardware provided better image stability. Further improvement is possible using commercial telescopic equipment that features more precisely engineered moving parts; however, this setup would require us to abandon our use of low-cost hardware that is easily accessible to hobbyists and citizen scientists.

Animal welfare statement

The authors report a field study which observes wild, free-living vertebrates in their natural environment without interaction. No animals were captured, handled, or excessively disturbed during this remote sensing experiment.

Supplementary data

Supplementary data available at *ICB* online.

Funding

This work was supported by the University of Oklahoma Aeroecology University Strategic Initiative, the University of Oklahoma Thousands Strong LunAero crowdfunding campaign, and the National Science Foundation award [grant number 1840230].

Author contributions statement

W.H. and E.B. conceived the experiment(s), W.H. conducted the experiment(s), and W.H. and E.B. analyzed the results. W.H. and E.B. wrote and reviewed the manuscript.

Acknowledgments

The authors thank the anonymous reviewers for their valuable suggestions. Some of the computing for this project was performed at the OU Supercomputing Center for Education & Research (OSCER) at the University of Oklahoma (OU).

Data availability statement

Data used in this paper are available through the Open Science Framework repository: https://osf.io/k7tjd/.

References

Andrews LC, Phillips RL, Hopen CY, Al-Habash MA. 1999. Theory of optical scintillation. J Opt Soc Am A: Opt Im Sci Vis 16:1417–29.

Bachmann S, Zrnić D. 2007. Spectral density of polarimetric variables separating biological scatterers in the VAD display. J Atmos Ocean Techn 24 1186–98.

Bradski G. 2000. The opencv library. Doc Dobbs J 25:11.

Carpenter FW. 1906. An astronomical determination of the heights of birds during nocturnal migration. Auk 23:210–17.

Chilson PB, Frick WF, Kelly JF, Howard KW, Larkin RP, Diehl RH, Westbrook JK, Kelly TA, Kunz TH. 2011. Partly cloudy with a chance of migration: weather, radars, and aeroecology. Bull Am Meteorol Soc 93:669–86.

Farnsworth A, Gauthreaux SA, van Blaricom D. 2004. A comparison of nocturnal call counts of migrating birds and reflectivity measurements on Doppler radar. J Avian Biol 35:365–69.

Fitzgibbon AW, Fisher RB. 1995. A buyer's guide to conic fitting. In: Pycock D, editor. Proceedings of the 6th British conference on machine vision 2: p. 513–522, Birmingham: BMVA Press.

Gauthreaux J, Sidney A. 1970. Weather radar quantification of bird migration. BioScience 20:17–19.

Gould WB. 1947. Radar reflections from the lower atmosphere. Proc IRE 35:1105–6.

Harper WG, Lack DL. 1958. Detection of bird migration by centimetric radar—a cause of radar 'angels'. Proc R Soc Lond. B - Biol Sci 149:484–502.

Honeycutt WT, Heaston AV, Kelly JF, Bridge ES. 2020. LunAero: automated "smart" hardware for recording video of nocturnal migration. HardwareX 7:e00106.

Horton KG, Nilsson C, Van Doren BM, La Sorte FA, Dokter AM, Farnsworth A. 2019. Bright lights in the big cities: migratory birds' exposure to artificial light. Front Ecol Environ 17:209–14.

Jenner E. 1824. II. Some observations on the migration of birds. By the late Edward Jenner, MDFRS; with an introductory letter to Sir Humphry Davy, Bart. Pres. RS By the Rev. GC Jenner. Phil Trans R Soc Lond. 1824:11–44.

KaewTraKulPong P, Bowden R. 2002. An improved adaptive background mixture model for real-time tracking with shadow detection. In: Remagnino P, Jones GA, Paragios N, Regazzoni CS. editors, Video-based surveillance systems: computer vision and distributed processing. Boston, (MA): Springer, p. 135–44.

Komenda-Zehnder S, Jenni L, Liechti F. 2010. Do bird captures reflect migration intensity?—Trapping numbers on an Alpine pass compared with radar counts. J Avian Biol 41:434–44.

Lack D, Varley GC. 1945. Detection of birds by radar. Nature 156:446.

Lakshmanan V, Karstens C, Krause J, Elmore K, Ryzhkov A, Berkseth S. 2015. Which polarimetric variables are important for weather/no-weather discrimination? J Atmos Ocean Techn 32:1209–23.

Liechti F, Bruderer B, Paproth H. 1995. Quantification of nocturnal bird migration by moonwatching: comparison with radar and infrared observations (Cuantificación de la Migración Nocturna de Aves Observando la Luna: Comparación con Observaciones de Radar e Intrarrojas). J Field Ornithol 66:457–68.

Lowery GH. 1951. A quantitative study of the nocturnal migration of birds 3. Lawrence, (KS): Univeristy of Kansas Publications.

Maddox RA, Zhang J, Gourley JJ, Howard KW. 2002. Weather radar coverage over the contiguous United States. Weather Forecast 17:927–34.

Møller AP, Szép T. 2011. The role of parasites in ecology and evolution of migration and migratory connectivity. J Ornithol 152:141–50.

Nisbet ICT. 1959. Calculation of flight directions of birds observed crossing the face of the moon. Wilson Bull 71:237–43.

Nisbet ICT. 1963. Quantitative study of migration with 23-centimetre radar∗. Ibis 105: 435–60.

O'Neal BJ, Stafford JD, Larkin RP. 2010. Waterfowl on weather radar: applying ground-truth to classify and quantify bird movements. J Ornitholy 81:71–82.

Oliphant TE. 2006. A guide to NumPy, 1. USA: Trelgol Publishing. https://numpy-discussion.scipy.narkive.com/tFhXG9WY/citing-numeric-and-numpy.

Osborn J, Föhring D, Dhillon VS, Wilson RW. 2015. Atmospheric scintillation in astronomical photometry. Mon Not R Astron Soc 452:1707–16.

Price-Whelan A.M, Sipőcz BM, Günther HM, Lim PL, Crawford SM, Conseil S, Shupe DL, Craig MW, Dencheva N et al. 2018.

The astropy project: building an open-science project and status of the v2.0 core package. Astron J 156:123.

Rhodes B, van Kerkwijk M., Davies J, Eichhorn H, Rodríguez J. 2019. JPLephem: jet propulsion lab ephemerides package. Astrophysics Source Code Library. https://ui.adsabs.harvard.edu/abs/2019ascl.soft08017R/abstract.

Richter S, Bick A. 2018. ROSTOCK: the zoological collection of the university of Rostock. In Beck LA, editor, Zoological collections of Germany: the animal kingdom in its amazing plenty at museums and universities, natural history collections. Cham: Springer International Publishing, p. 583–89.

Robitaille TP, Tollerud EJ, Greenfield P, Droettboom M, Bray E, Aldcroft T, Davis M, Ginsburg A, Price-Whelan A.M et al., 2013. Astropy: a community python package for astronomy. 558:A33.

Russell KR, Mizrahi DS, Gauthreaux SA. 1998. Large-scale mapping of purple martin pre-migratory roosts using WSR-88D weather surveillance radar (mapas a larga escala de los dormideros pre-migratorios de Progne subis Utilizando radares WSR-88D Para el Monitoreo del Clima). J Field Ornithol 69:316–25.

Scott WED. 1881. Some Observations on the Migration of Birds. Bull Nuttall Ornithol Club 6:97–100.

Somveille M, Rodrigues ASL, Manica A. 2015. Why do birds migrate? A macroecological perspective. Global Ecol Biogeogr 24:664–74.

Suzuki S, be K. 1985. Topological structural analysis of digitized binary images by border following. Comput Vision Graph Image Process 30:32–46.

Winkler DW. 2006. Roosts and migrations of swallows. Hornero 21:85–97.

Zaugg S, Saporta G, van Loon E, Schmaljohann H, Liechti F. 2008. Automatic identification of bird targets with radar via patterns produced by wing flapping. J R Soc Inter 5:1041–53.